Published in final edited form as:

J Am Chem Soc. 2022 December 21; 144(50): 23030–23043. doi:10.1021/jacs.2c10029.

3D orientation imaging of polymer chains with polarization-controlled coherent Raman microscopy

Shuyu Xu,

Biosystems and Biomaterials Division, National Institute of Standards and Technology, Gaithersburg, Maryland 20899, United States

Ying Jin,

Biosystems and Biomaterials Division, National Institute of Standards and Technology, Gaithersburg, Maryland 20899, United States

Young Jong Lee

Biosystems and Biomaterials Division, National Institute of Standards and Technology, Gaithersburg, Maryland 20899, United States

Abstract

Despite the ubiquity of three-dimensional (3D) anisotropic materials, their 3D molecular alignment cannot be measured using conventional two-dimensional (2D) polarization imaging. Here, we present images of the 3D angles of molecular orientations with submicrometer spatial resolution acquired through polarization-controlled coherent anti-Stokes Raman scattering microscopy. The hyperspectral Raman data of a polyethylene (PE) film were converted into images showing the polymer chains' 3D angles and order parameters. The 3D orientation images of PE chains in ring-banded spherulites show that the azimuthal angles of the chains are perpendicular to the crystal growth direction, while the out-of-plane angles display limited-range oscillations synchronous with ring banding. The prevailing crystal growth model of fully twisting lamellae is inconsistent with the observed restricted oscillations of the out-of-plane direction, which are unobservable through conventional 2D projected imaging. This high-resolution, label-free, quantitative imaging of 3D molecular orientation can become a standard measurement tool for the microscopic structures of complex synthetic and biological materials.

Corresponding Author youngjong.lee@nist.gov.

Competing interests

The authors declare no competing interests.

The authors declare no competing financial interest.

Certain commercial equipment, instruments, or materials are identified in this paper to foster understanding. Such identification does not imply endorsement by NIST, nor does it imply that the materials or equipment identified are necessarily the best available for the purpose.

ASSOCIATED CONTENT

Supporting Information. The Supporting Information is available free of charge at http://pubs.acs.org/doi/.

Confocal *xz*-image of the HDPE film; polarization dependence of the narrowband beam; Im$\{\chi^{(3)}\}$ as a function of polarization angle and distance on line ***N*** and line ***B***; simulation of a (B_{1g}+B_{2g}) degenerate peak; effect of $\langle P_2\rangle$–$\langle P_4\rangle$ model on the orientation results; effect of tight focusing on a nonlinear susceptibility; comparison of $|\theta|$ for two (B_{1g}+B_{2g}) peaks at 1060 and 1294 cm^{-1}; illustrations of the chain orientations based on the restricted oscillation model and the full twist model; effect of spatial resolution on the observed $|\theta|$; table of Raman tensor elements; and SI References.

INTRODUCTION

Three-dimensional (3D) anisotropic molecular alignment and the associated anisotropy occur commonly in natural and synthesized materials at several structural levels, defining the physical, chemical, and biological properties. Accurate measurements of molecular orientation with high spatial resolution are critical for understanding the relationship between the microscopic structure and macroscopic properties and for controlling and improving material performances. However, there is no quantitative measurement technique of 3D molecular orientation for continuously distributed organic materials with submicrometer spatial resolution. For example, when polymers become crystallized, they form a hierarchical and anisotropic structure, including unit cells, lamellar stacks, and spherulitic domains, where a pattern of concentric rings is often observed. The mechanisms of the ring banding phenomenon have been extensively studied, and a fully twisting lamellar model has been considered as the prevailing mechanism.[1–3] However, fully twisting lamellae were observed only in isolated forms,[4,5] but full 360° twisting has never been directly measured from intact polymer films due to the absence of appropriate quantitative imaging methods for 3D orientation.

Various imaging methods have been developed to map the molecular orientation in spatially heterogeneous materials. The 3D orientation of single crystals can be determined by X-ray diffraction (XRD). X-ray diffraction-based microscopy has been used to determine the orientations of separate crystallite domains in polycrystalline materials.[6,7] However, X-ray tomographic imaging is limited to studying highly crystalline samples with a thickness of at least tens of micrometers, and its spatial resolution is limited to several micrometers. Due to weak scattering cross section, X-ray based orientational imaging of organic materials requires a synchrotron source, which is not readily available. Electron diffraction can be used to map the crystallographic orientation with a higher spatial resolution either by the backscatter diffraction in a scanning electron microscope or the selected-area diffraction in a transmission electron microscope.[8,9] However, due to the limited penetration depth of electrons, only the shallow surfaces or thin foils (<100 nm) can be investigated by electron diffraction microscopy. Charge accumulation and beam damage are still challenging problems for high-resolution imaging of organic materials, including polymers.[10]

Alternatively, optical imaging techniques have been widely used to nondestructively map the anisotropy of the samples and determine the molecular orientation. Optical imaging of the anisotropy is typically based on linearly polarized optical systems, such as fluorescence,[11,12] second harmonic generation,[13] infrared (IR) absorption,[14–16] and Raman scattering.[17–21] However, polarization optical microscopy methods can only measure the 2D projection of molecular orientation onto the polarization plane but cannot determine the out-of-plane angle of molecules in 3D. Due to the inability to measure the out-of-plane angle, the 2D projected orientation measurement can characterize the orientational distribution function properly only when the sample symmetry axis can be assumed to lie in the polarization plane, such as fibers and highly stretched films.[22,23] Different imaging approaches based on radially polarized excitation were reported to detect the signal difference between longitudinally and transversely aligned molecules in spontaneous and coherent Raman microscopies.[24,25] However, the simple ratio of radial and transverse Raman intensities

could not be converted into the out-of-plane angle without knowing the molecular twisting angle and the orientational broadening.[26]

Other high-resolution optical imaging methods have been demonstrated to measure the 3D orientation angles of isolated molecules by analyzing finely *z*-scanned defocused images,[27] comparing with point spread functions,[28] or detecting emissions from 2D-degenerate fluorophores.[29] However, those exquisite methods are inappropriate for continuously distributed materials, such as polymers and tissues.

Recently, a spectral analysis method, called the orthogonal-pair polarization IR (OPPIR), was proposed to determine 3D angles of molecular orientation by concurrently analyzing two orthogonal IR modes.[30] The new method was experimentally demonstrated with a semicrystalline polymer film and the structural change induced by shear deformation.[31,32] However, the diffraction limit of IR microscopy is several micrometers, which is often not sufficient to resolve microscopic orientational variations.

Compared to IR microscopy, Raman imaging can provide an order of magnitude higher spatial resolution with sectioning capability. Earlier, polarization Raman microscopy was used to determine the 3D orientation of single crystals, polycrystals, and nanowires.[33–35] These materials were characterized by a small number of Raman peaks and their large Raman cross sections. More importantly, the polarization analysis was focused on a single Raman peak whose triple-degenerated polarizability tensors were exploited with respect to the 3D angles of crystal orientation. In contrast to inorganic crystals with high crystallinity, Raman spectra of organic materials are not only more crowded but also more readily affected by orientational broadening and amorphous contributions. Thus, analyzing a single Raman peak (e.g., the amide I peak) cannot yield the 3D orientation angles without a priori knowledge of the Raman tensor elements and the orientational broadening,[36,37] which are not trivial to measure independently at the exact location of the sample. As opposed to those single Raman peak analyses, an algorithm based on two Raman peaks was theoretically proposed to determine the 3D orientation angles,[38] which is similar to the OPPIR method for IR imaging.[31,32] However, the proposed algorithm was based on the assumption that the polarizability tensors must have a single nonzero diagonal element, which is impractical for typical organic molecules, unfortunately.

This paper introduces a new algorithm to determine the 3D orientation angles of molecular orientation using hyperspectral Raman images obtained by polarization-controlled broadband coherent anti-Stokes Raman scattering (BCARS) microscopy. In principle, equivalent polarization Raman information can be collected by BCARS and spontaneous Raman. However, BCARS can provide a faster imaging speed than spontaneous confocal Raman, which can be more advantageous in these multidimensional hyperspectral images repeated at multiple polarization angles. We investigated a high-density polyethylene (HDPE) film, one of the most produced commodity polymer materials. A multiple-annealed, slowly cooled, thin PE film sandwiched between coverslips was imaged with a BCARS microscope at various polarization angles of the excitation lights. Thanks to the earlier extensive studies of the Raman polarizabilities of PE,[39–42] we were able to determine the 3D orientation angle and the order parameter of polymer chains with submicrometer spatial

resolution. We identified a Raman peak with degenerate symmetries that can be used to determine the axial angle of the orientation by assuming an analytical relation between the second- and fourth-order parameters. In this paper, we determined the azimuthal angle, the axial angle, and the order parameters at each image pixel and mapped the orientations on two lines across a nucleation center and a spherulite boundary. We discussed the observed orientation maps of PE chains with respect to ring banding periods and the related lamellar twisting mechanisms.

EXPERIMENTAL METHODS

Sample Preparation.

A thin HDPE film was prepared for imaging. A stock HDPE (NIST SRM1475, mass-average molar mass = 53000 g/mol, dispersity = 2.9) strip was first melted at 170 °C for 5 min under pressure. The film was sandwiched between two glass coverslips and pressed with two aluminum blocks by a spring clamp. Then, the sandwiched film was reheated at 170 °C for 1 h, annealed at 124 °C for 18 h, and cooled to room temperature slowly overnight in a vacuum. The HDPE film was imaged as the intact sandwiched form between the two glass coverslips. From an *XZ*-scanned confocal image of the film cross section (see Figure S1), the film thickness was estimated to be 2.1 μm. Based on DSC reports of slow-melt crystalized HDPE films made from NIST SRM1475, the crystallinity of the sample was estimated to be (74–88%).[43,44]

Polarization-Controlled BCARS Microscopy.

The imaging system, illustrated in Figure 1a, was based on the polarization-controlled beam scanning BCARS microscopy setup.[45,46] Briefly, a fundamental laser beam from a Ti:Sapphire femtosecond oscillator (MaiTai, Spectra-Physics), centered at 830 nm, was split into two beams. One beam was spectrally narrowed to 1 nm bandwidth by a 4-*f* dispersionless filter. The other beam was converted to a continuum light ranging from 850 to 1150 nm by a photonic crystal fiber (PCF, Femtowhite, NKT Photonics). The two beams were combined and directed collinearly toward the sample. The polarization of the two beams was linear and parallel by passing through a polarizer (Pol1). The polarization angle was rotated by an achromatic half-wave plate (HWP1, AHWP05M-980, Thorlabs) mounted in a motorized rotation stage. The excitation beams were subsequently focused onto a sample through an objective lens (40×, numerical aperture (NA) 0.95, Olympus). The laser powers measured at the sample location were approximately 17 and 11 mW for the narrowband and the continuum, respectively. CARS signals were collected by an objective lens (60×, NA 0.7, Olympus) in the forward direction. The polarization angle of the signals was rotated back by another set of an achromatic half-wave plate (HWP2, AHWP05M-600, Thorlabs) and a polarizer (Pol2). Pol2 was aligned parallel to Pol1, and HWP2 was rotated synchronously to HWP1 so that only the signals became parallel to Pol2. The CARS signal was analyzed by a monochromator (SCT-320, Princeton Instruments) equipped with a charge-coupled device (CCD, 1024×256 pixels, DU920-BRDD, Andor). BCARS hyperspectral data were collected in two imaging modes. For imaging a large area of fixed polarization excitation, the sample-scanning mode was used, where the full vertical binned CCD signals were recorded per image pixel while the sample was moved.

For collecting polarization-resolved analysis, the beam scanning mode was used, where the BCARS spectra of a line segment illuminated by a scanning mirror (SM) were recorded while the polarization angle was rotated.

The signal wavelength detected by the CCD ranged from 850 to 700 nm, corresponding to the Raman shift from –500 to +4000 cm^{-1}. The short pass filter in front of the monochromator reduced the excitation light significantly, but the intense narrowband beam was still detectable. The narrowband beam intensity was used for the alignment of Pol1, Pol2, HWP1, and HWP2. At a blank location without HDPE, the narrowband intensity was monitored while HWP1 and HWP2 were synchronously rotated. Figure S2 shows that the polarization-dependent intensity varied only by a 1.1% standard deviation. A separate measurement with an isotropic liquid sample (glycerol) in the place of the polymer film shows 1.0% standard deviation, indicating that most of the polarization dependence is not due to the system's polarization dependence and the film's birefringence and diattenuation.

Spectral Image Processing.

A raw BCARS spectrum, I_{CARS}, was converted to the imaginary component of the third-order nonlinear susceptibility, $\mathrm{Im}\{\chi^{(3)}\}$, by the Kramer–Kronig (KK) phase retrieval.[47,48] The spectrum of $\mathrm{Im}\{\chi^{(3)}\}$, equivalent to the spontaneous Raman spectrum, was further analyzed for various polarization angles. Each KK-retrieved spectrum was fitted with multiple Gaussian functions. While the center frequency and the bandwidth were fixed for each underlying peak, the amplitude was adjusted for the best fit.

RESULTS AND DISCUSSION

Polarization-Dependent BCARS and Retrieval of $\mathrm{Im}\{\chi^{(3)}\}$.

Figure 1b,c show bright-field and polarization optical microscopy (POM) images, respectively, of the identical region of an HDPE film. While the bright-field image looks featureless, the POM image of the identical area shows well-defined spherulites featured by concentric rings and the Maltese cross. The high-resolution confocal scattering image in Figure 1d shows that the rings consist of lathlike sub-features that are cooperatively banded.

The microscopic optical anisotropy was also observable in polarization-controlled CARS spectra. The generated CARS signal, I_{CARS}, is proportional to $|\chi^{(3)}|^2 = |\chi_r^{(3)} + \chi_{NRB}^{(3)}|^2$, where $\chi_r^{(3)}$ is the vibrationally resonant susceptibility and $\chi_{NRB}^{(3)}$ is the nonresonant background (NRB) susceptibility. Because of the interference between $\chi_r^{(3)}$ and $\chi_{NRB}^{(3)}$, the spectral shape of I_{CARS} looks dispersion-like, and the spectral analysis becomes complicated. We used the KK phase retrieval method to eliminate the $\chi_{NRB}^{(3)}$ contribution and retrieve the imaginary component of $\chi^{(3)}$, or $\mathrm{Im}\{\chi^{(3)}\}$.[47] Because $\mathrm{Im}\{\chi^{(3)}\}$ is proportional to the spontaneous Raman cross section,[49] the symmetry and tensor of a Raman mode can be referenced from studies by spontaneous Raman spectroscopy. Figure 1e,f shows the $\mathrm{Im}\{\chi^{(3)}\}$ spectra measured at a single pixel, excited by different polarization angles. Raman peaks in the $\mathrm{Im}\{\chi^{(3)}\}$ spectra show different polarization dependence from each other.

Polarization-Dependent BCARS Images of HDPE Spherulites.

Figure 2 shows the Im$\{\chi^{(3)}\}$ images of the HDPE film at four different frequencies by *X*- and *Y*-polarized excitations. In Figure 2c,d, the Im$\{\chi^{(3)}\}$ images of the ν_s(C–C) mode at 1126 cm^{-1} are featured by a bow tie shape perpendicular to the polarization direction. Concentric undulations due to ring banding are unambiguously observable. In contrast, the Im$\{\chi^{(3)}\}$ images of the $\nu_s(CH_2)$ mode at 2846 cm^{-1} in Figure 2g,h show that a bow tie is aligned parallel to the polarization direction. The ring banding pattern becomes unclear in the bright area but weakly observable in the dark area. The images of $\delta(CH_2)$ at 1440 cm^{-1} in Figure 2e,f show different patterns from the other two images. A diagonal cross shape appears brighter with well-defined ring banding patterns in the cross arms. In Figure 2i,j, the composite of the three Im$\{\chi^{(3)}\}$ images shows that the three Raman modes complement each other. For example, the ring banding patterns of the $\nu_s(CH_2)$ mode (red) and the $\delta(CH_2)$ mode (green) are out-of-phase with each other.

All images in Figure 2 show a mirror symmetry with respect to the polarization direction for both polarization directions, indicating that the overall molecular alignment in the spherulite is radially symmetrical. Earlier, Lee et al. observed similar bow tie and diagonal cross patterns from polarization BCARS images of an HDPE/LLDPE homopolymer blend.[19] They described the unique polarization-dependent features of PE spherulites using a collective twisting lamellar model by focusing on the two Raman modes. For example, let us consider full and smooth lamellae twisting per ring banding period only along the *X* axis from the nucleation center. Then, the direction of PE chains, perpendicular to lamellae, will alternate between the film's normal direction (*Z* axis) to the tangential direction of the ring banding (*Y* axis). Then, the ν_s(C–C) mode, which dominantly represents the PE main chain direction, will become bright and dark alternatively by the *Y*-polarized excitation (Figure 2c) but will remain dark by the *X*-polarized excitation (Figure 2d). In contrast, the $\nu_s(CH_2)$ mode plane, which is assumed to be perpendicular to the main chains, will alternate between the *XY* and *XZ* planes. Then, the $\nu_s(CH_2)$ mode will become constantly bright by the *X*-polarized excitation (Figure 2h) and alternate between medium and dark by the *Y*-polarized excitation (Figure 2g). However, these qualitative discussions were based on assumptions that the polarizability tensor of the ν_s(C–C) mode has only one nonzero element on the chain axis and that the polarizability tensor of the $\nu_s(CH_2)$ mode contains only two identical nonzero elements on the CH_2 plane axes. In the following sections, we will analyze the polarization angle dependence of Im$\{\chi^{(3)}\}$ signals using Raman tensors for multiple Raman symmetries. We will focus on two line scans to demonstrate the determination of the 3D orientation angles of the PE chain direction. As shown in Figure 2i,j, one line (labeled as ***N***) crosses a nucleation center, while the other line (labeled as ***B***) crosses a boundary between spherulites. Both lines cross multiple banded rings; thus, we will see how the 3D chain orientation varies with ring banding.

Polarization Profiles of Various Raman Peaks.

Figure 3 shows contour images of Im$\{\chi^{(3)}\}$ at eight representative frequencies as a function of polarization angle and distance along line ***N*** (the top panel) and line ***B*** (the bottom panel). All contour images show periodic polarization dependence at all *X* locations. Most peaks show an angular period of 180° while peaks at 1461 and 1440 cm^{-1} (in Figure S3) show

a period of 90°. Interestingly, the polarization dependence of the different Raman modes shows close symmetry angles to each other. In Figure S3i–l and S3u–x, the polarization profiles from a single image pixel show more clearly the periodicities and the proximity of the symmetry angles among the Raman modes.

More specifically, the 1060 and 1294 cm^{-1} peaks are similar in shape, showing a doughnut-like feature per ring banding. In contrast, the 1126 and 1416 cm^{-1} peaks show no doughnut-like features. The 1126 cm^{-1} peak shows a wide band with a period of 180°, while the 1416 cm^{-1} peak shows the main band and a weaker out-of-phase band. The 2846 and 2878 cm^{-1} peaks appear at an angle shifted by 90° from the 1126 and 1416 cm^{-1} peaks. The 2846 cm^{-1} peak shows a wide band, while the 2878 cm^{-1} peak shows the main band and an additional weaker band. Also, the 2846 and 2878 cm^{-1} peaks look more continuous along with ring banding than the other peaks. Overall, the polarization-dependent features, such as the doughnut-like pattern, appear repeatedly per ring banding, indicating that chain orientation changes within a ring banding period and repeats over multiple periods. Also, the similarity in the polarization dependence between line ***N*** and line ***B*** suggests that the molecular alignment is similar between the central and distal areas of a spherulite.

Nonlinear susceptibility tensors and Raman polarizability tensors.

In general, CARS intensity can be expressed as

$$I_{\mathrm{CARS}} \propto \left|\boldsymbol{P}^{(3)}\right|^2 \propto \left|\boldsymbol{\chi}^{(3)}\boldsymbol{E}^{\mathrm{pu}}\boldsymbol{E}^{\mathrm{S}*}\boldsymbol{E}^{\mathrm{pr}}\right|^2 \tag{1}$$

where $\boldsymbol{P}^{(3)}$ is the generated nonlinear polarization of the anti-Stokes signal; $\boldsymbol{\chi}^{(3)}$ is the fourth-rank tensor of the third-order nonlinear susceptibility; and $\boldsymbol{E}^{\mathrm{pu}}$, $\boldsymbol{E}^{\mathrm{S}}$, and $\boldsymbol{E}^{\mathrm{pr}}$ are the electric field vectors of the pump, Stokes, and probe transitions, respectively. In this study, the excitation electric fields are defined by a specific polarization angle, and the CARS signal of the same polarization component is detected. Then, the polarization-resolved I_{CARS} can be expressed as $I_{\mathrm{CARS}}(\eta) \propto \left|P^{(3)}_{\mathrm{eff}}(\eta)\right|^2$, where the effective nonlinear polarization is defined as $P^{(3)}_{\mathrm{eff}}(\eta) \equiv \boldsymbol{P}^{(3)}(\eta)\cdot\hat{\boldsymbol{e}}(\eta)$, where η is the polarization angle and $\hat{\boldsymbol{e}}(\eta) = (\cos\eta, \sin\eta, 0)$ is the unit vector representing the polarization direction. If the electric fields are expressed in a form that separates the amplitude, E, and the direction, as $\boldsymbol{E}(\eta) = E\hat{\boldsymbol{e}}(\eta)$, the effective nonlinear polarization can be expressed with the effective third-order nonlinear susceptibility, $\chi^{(3)}_{\mathrm{eff}}(\eta)$, as

$$\begin{aligned} P^{(3)}_{\mathrm{eff}}(\eta) &= \left\{\sum_{IJKL} e_I(\eta)\chi^{(3)}_{IJKL}e_J(\eta)e_K(\eta)e_L(\eta)\right\}E^{\mathrm{pu}}\ E^{\mathrm{S}*}\ E^{\mathrm{pr}} \\ &= \left\{\chi^{(3)}_{\mathrm{eff}}(\eta)\right\}E^{\mathrm{pu}}\ E^{\mathrm{S}*}\ E^{\mathrm{pr}} \end{aligned} \tag{2}$$

where $(I, J, K, L) \in (X, Y, Z)$ in the laboratory frame.

The macroscopic third-order nonlinear susceptibility fourth-rank tensor, $\chi^{(3)}_{IJKL}$, is independent of η but dependent on the orientation angles of probed molecules. The macroscopic value defined in the laboratory frame needs a coordinate rotation to be

connected to its microscopic third-order nonlinear susceptibility fourth-rank tensor, $\gamma^{(3)}_{ijkl}$, where (i, j, k, l) ∈ (a, b, c) in the molecule or lattice frame. The Euler rotation matrix, $\mathbf{R}(\psi,\phi,\theta)$, can be used to represent the coordinate rotation. ψ, ϕ, and θ are the azimuthal angle, rotational angle, and axial angle, respectively. Then,

$$\chi^{(3)}_{IJKL}(\psi,\theta,\phi) = N\sum_{ijkl}(R_{Ii}R_{Jj}R_{Kk}R_{Ll})\gamma^{(3)}_{ijkl} \quad (3)$$

where R_{Xx} are the (X, x) element of $\mathbf{R}(\psi,\phi,\theta)$, and all N molecules are assumed to be oriented parallel to each other (the oriented gas model). More accurately, the orientational distribution function of the molecules must be used. We will discuss the broadening effect qualitatively later in this paper.

Because the CARS signal generation is a four-wave mixing process, its nonlinear susceptibility can be expressed as a product of two second-rank tensors corresponding to two Raman polarizabilities for the pump/Stokes and the probe/anti-Stokes transitions. In the molecular frame, $\gamma^{(3)}_{ijkl}$ can be expressed as a product of molecular Raman tensors, $\boldsymbol{a}$. However, because a majority of HDPE chains exist in the crystalline phase, we consider a unit-cell Raman tensor, $\boldsymbol{a}'$, and its orientation in the laboratory frame, as illustrated in Figure 4. Then, eq 3 can be rewritten as

$$\chi^{(3)}_{IJKL}(\psi,\theta,\phi) \propto \sum_{ijkl}(R_{Ii}R_{Jj}R_{Kk}R_{Ll})\alpha'_{ij}\alpha'_{kl} \quad (4)$$

For a given Raman mode, the observed $\mathrm{Im}\{\chi^{(3)}\}(\eta)$ will correspond to $\chi^{(3)}_{\mathrm{eff}}(\eta)$, and eqs 2 and 4 will yield

$$\chi^{(3)}_{\mathrm{eff}} \propto \sum_{IJKL}\sum_{ijkl}(R_{Ii}R_{Jj}R_{Kk}R_{Ll}e_Ie_Je_Ke_L)\alpha'_{ij}\alpha'_{kl} \quad (5)$$

If relative values of tensor elements α'_{ij} are known priorly, $\mathrm{Im}\{\chi^{(3)}\}(\eta)$ will provide information on the orientation angles from (R_{Ii} R_{Jj} R_{Kk} R_{Ll}). On the other hand, if the molecular orientation angles are known by any other techniques, the tensor elements α'_{ij} of the probed Raman mode can be determined.

Table 1 shows the Raman symmetries of the representative Raman peaks of a PE unit cell based on the orthorhombic crystal phase.[39,41] A_g, B_{1g}, B_{2g}, and B_{3g} are the four Raman symmetries allowed for the unit cell point group D_{2h}. Most Raman peaks are observed in the degenerate form of two symmetries, such as (A_g + B_{3g}) and (B_{1g} + B_{2g}), except the δ(CH_2) peak for A_g. Some high-resolution studies of low-temperature samples showed that the peaks were separated by a few wavenumbers.[39] However, the room-temperature measurement with the limited spectral resolution (≈10 cm^{-1}) could not resolve the overlapping peaks. Then, the observed $\mathrm{Im}\{\chi^{(3)}\}$ can be considered as the $\chi^{(3)}_{\mathrm{eff}}$ sum of the degenerate peaks.

The Raman polarizability tensor, $\boldsymbol{\alpha}'$, for all four symmetries can be expressed in the 3×3 matrix form with respect to the (a, b, c) coordinate. The $\boldsymbol{\alpha}'$ for the A_g symmetry has three non-zero diagonal elements: α'_{aa}, α'_{bb}, and α'_{cc}. The other tensors for B_{1g}, B_{2g}, and B_{3g} symmetries have only one pair of non-zero off-diagonal elements, and the element pairs can be further simplified by $\alpha'_{bc} = \alpha'_{cb}$, $\alpha'_{ac} = \alpha'_{ca}$, and $\alpha'_{ab} = \alpha'_{ba}$, respectively. Based on the simplified tensors, $\chi^{(3)}_{\text{eff}}$ can be analytically expressed as a function of polarization angle and orientation angle. Table 2 shows the Raman polarizability in the matrix form of the four symmetry modes and their analytical expressions of $\chi^{(3)}_{\text{eff}}$.

(B_{1g} + B_{2g}) Mode.

As shown in Table 2, the expression of a (B_{1g} + B_{2g}) peak requires only two elements, e and f. Even the two elements are associated by the setting angle of PE chain planes with respect to the a axis (or b axis) in the unit cell.[39] The reported setting angles for orthorhombic PE are within a narrow range of (45 ± 4°).[51,52] Thus, we assume that $e = f$ for the Raman polarizabilities of the degenerate B_{1g} and B_{2g} modes. Then, the polarization dependence of a (B_{1g} + B_{2g}) peak can be expressed with only one independent tensor element: e (= f), and the expression of $\chi^{(3)}_{\text{eff}}$ can be simplified as

$$\begin{aligned}\chi^{(3)}_{\text{eff}}(B_{1g} + B_{2g}) &= \chi^{(3)}_{\text{eff}}(B_{1g}) + \chi^{(3)}_{\text{eff}}(B_{2g}) \\ &= k\left[\cos^2(\eta - \psi)\sin^2\theta - \cos^4(\eta - \psi)\sin^4\theta\right]\end{aligned} \tag{6}$$

where k is a proportional coefficient. It is noted that $\chi^{(3)}_{\text{eff}}$ (B_{1g} + B_{2g}) in eq 6 is not affected by ϕ, as shown in Figure S4. In the absence of orientational broadening, $\chi^{(3)}_{\text{eff}}$ (B_{1g} + B_{2g}) contains only two cosine terms with the same phase. The common phase of the two terms will yield ψ. The coefficient ratio of the two terms will lead to θ. This separate usage of the phase and the coefficients to determine ψ and θ will be similar to a system in the presence of orientational broadening, which will be explained in the following section.

A_g Mode.

We consider the peak at 1416 cm^{-1} because the nondegenerated A_g mode is expressible with a fewer number of tensor elements than the degenerated (A_g + B_{3g}) modes for other peaks. Similar to the derivation of eq 6, we assumed that the setting angle is 45° ($p = q$, in Table 2). Then, the expression of $\chi^{(3)}_{\text{eff}}$ for an A_g mode can be simplified as

$$\begin{aligned}\chi^{(3)}_{\text{eff}}(A_g) &= k'\left[\cos^2(\eta - \psi)\sin^2\theta - \left(\frac{p}{r - p}\right)\right]^2 \\ &= k'\left[\cos^2(\eta - \psi)\sin^2\theta - s'\right]^2\end{aligned} \tag{7}$$

where k' is a proportional coefficient. The parameter, s' = p/(r–p), is independent of chain orientation. Because the Raman peak at 1416 cm^{-1} is observed only with the crystalline PE and alkanes, the intensity ratio of 1416 cm^{-1} relative to 1294 cm^{-1} has often been used for quantifying the crystallinity of PE.[53] However, eqs 6 and 7 clearly show that the

Raman intensities of both peaks can vary with polarization angle and chain orientation. Thus, the Raman spectroscopic method for determining the crystallinity must be used with great care. Back to eq 7, the amplitude contains three parameters $\sin^2\theta$, k', and s', making it complicated. It becomes extremely challenging to solve the equations analytically from an observed polarization profile. In addition to the computational complexity, the proximity of the 1416 cm^{-1} peak to the neighboring peaks at 1440 and 1461 cm^{-1} makes quantitative analysis practically challenging.

Orientational Broadening.

When molecular orientation is broadened uniaxially around the mean orientation direction, eq 6 for a (B_{1g} + B_{2g}) peak will be modified as an integral form defined by an orientational distribution function (ρ) with broadening angles (β and γ) as

$$\langle \chi^{(3)}_{\text{eff}}(B_{1g} + B_{2g})\rangle = k\int_0^{2\pi}\int_0^{\pi}[\cos^2(\eta-\psi')\sin^2\theta' - \cos^4(\eta-\psi')\sin^4\theta']\rho(\beta,\gamma)\sin\beta \mathrm{d}\beta\mathrm{d}\gamma \tag{8}$$

where ψ' and θ' are the azimuthal and axial angles of an orientationally broadened chain; $\rho(\beta,\gamma)$ is the orientational distribution function; and β and γ are the axial and the azimuthal angles from the mean orientational axis. If we assume that the orientational distribution function is uniaxially symmetrical, $\rho(\beta,\gamma)$ can be reduced to $\rho(\beta)$. Then, eq 8 can be integrated by γ and yield $\cos^2\beta$ and $\cos^4\beta$ terms. The integrals of $\cos^2\beta$ and $\cos^4\beta$ can be simplified by using the second and fourth-order parameters, $\langle P_2\rangle$ and $\langle P_4\rangle$,[42]

$$\int_0^{\pi}\cos^2\beta\rho(\beta)\sin\beta d\beta = \frac{2}{3}\langle P_2\rangle + \frac{1}{3}$$
$$\int_0^{\pi}\cos^4\beta\rho(\beta)\sin\beta d\beta = \frac{8}{35}\langle P_4\rangle + \frac{4}{7}\langle P_2\rangle + \frac{1}{5} \tag{9}$$

Then, eq 8 can be expressed without integrals as

$$\langle \chi^{(3)}_{\text{eff}}(B_{1g} + B_{2g})\rangle = k[\cos^2(\eta-\psi)\sin^2\theta\left(\frac{6}{7}\langle P_4\rangle + \frac{1}{7}\langle P_2\rangle\right) - \cos^4(\eta-\psi)\sin^4\theta\langle P_4\rangle + \left(-\frac{3}{35}\langle P_4\rangle - \frac{1}{21}\langle P_2\rangle + \frac{2}{15}\right)] \tag{10}$$

The basic form of eq 10 is similar to eq 6. The differences are the reduced coefficients of the $\cos^2(\eta-\psi)$ and $\cos^4(\eta-\psi)$ terms and the offset. It is noted that the phases of the two cosine terms are not changed by broadening; thus, the azimuthal angle can be determined by $\psi = \eta_{\text{min}} + 90°$, similar to eq 6. However, θ cannot be determined directly from the ratio of the coefficients of the $\cos^2(\eta-\psi)$ and $\cos^4(\eta-\psi)$ terms without knowing $\langle P_2\rangle$ and $\langle P_4\rangle$ values. Then, eq 10 can be re-expressed using three simplified coefficients as

$$\langle \chi^{(3)}_{\text{eff}}(B_{1g} + B_{2g})\rangle = m\cos^2(\eta-\psi) - n\cos^4(\eta-\psi) + l \tag{11}$$

where the coefficients are

$$m = k \sin^2\theta\left(\frac{6}{7}\langle P_4\rangle + \frac{1}{7}\langle P_2\rangle\right) \tag{12}$$

$$n = k \sin^4\theta\langle P_4\rangle \tag{13}$$

$$l = k\left(-\frac{3}{35}\langle P_4\rangle - \frac{1}{21}\langle P_2\rangle + \frac{2}{15}\right) \tag{14}$$

The phase angle and the three coefficients (m, n, and l) can be determined by fitting an experimentally observed polarization profile of the $\chi^{(3)}_{\text{eff}}(B_{1g} + B_{2g})$ peak. Using the fitting results, we determine ψ from the phase angle and then, θ, $\langle P_2\rangle$, and $\langle P_4\rangle$ from the other fitting coefficients. It must be noted that the expressions with $\langle P_2\rangle$ and $\langle P_4\rangle$ in eqs 10–14 are based on a uniaxial symmetry for $\rho(\beta)$. It is also noted that $\rho(\beta)$ is defined within an image pixel and can vary with the probed volume or the spatial resolution of the imaging system.

Combining eqs 12 and 13 eliminates k as

$$\sin^2\theta = \frac{n}{m}\left(\frac{6}{7} + \frac{1}{7}\frac{\langle P_2\rangle}{\langle P_4\rangle}\right) \tag{15}$$

Then, rearranging eqs 12–14 yields

$$\frac{n \times l}{m^2} = \frac{7}{15}\frac{\langle P_4\rangle(-9\langle P_4\rangle - 5\langle P_2\rangle + 14)}{(6\langle P_4\rangle + \langle P_2\rangle)^2} \tag{16}$$

Because this single equation still contains two unknowns, $\langle P_2\rangle$ and $\langle P_4\rangle$, solving eq 16 requires an additional constraint between the two unknown variables.

Determination of ψ.

Figure 5c,h shows the polarization profiles of Im$\{\chi^{(3)}\}$ at 1294 cm^{-1} and 1126 cm^{-1} acquired at several locations marked in Figure 5a,b and Figure 5f,g, respectively. At all locations, the polarization profiles of both Raman modes show twofold mirror symmetry and share their symmetry axes between the two Raman modes. Since the polarization profile of (B_{1g} + B_{2g}) peaks can be expressed in a relatively simple analytical form even with an orientational broadening (eqs 10 and 11). Also, the peak at 1294 cm^{-1} is farther separated from its neighboring peaks than other Raman peaks; thus, we used the 1294 cm^{-1} peak to determine ψ. The phase angle of the $\cos^2(\eta - \psi)$ and $\cos^4(\eta - \psi)$ terms can yield ψ. In Figure 5d, the ψ plot along line ***N*** shows that ψ values remain close to 90° without any significant change. The relatively constant ψ at 90° indicates that the projection of PE chains in Figure 5e is tangential to the banded rings and perpendicular to the crystal growth direction. In contrast, in Figure 5i, the ψ values change with the position on line ***B*** and show different slopes on the two sides across the boundary. However, the projected chain

orientation in Figure 5j still perpendicular to the crystal growth directions of two colliding spherulites.

Determination of ϕ.

From eqs 6 and 8, $\chi^{(3)}_{\text{eff}}$ of a (B_{1g} + B_{2g}) peak is not affected by ϕ. On the other hand, the polarization profile of a (A_g + B_{3g}) peak can vary with ϕ according to Table 2. Figure 6a–f shows the $\chi^{(3)}_{\text{eff}}$ polar plots of six (A_g + B_{3g}) peaks simulated using the Raman tensor elements of orthorhombic *n*-alkane.[39] The tensor elements used for the simulation are listed in Table S1. The simulated polarization profiles of some Raman modes (1126, 1416, 2846 cm^{-1}) are less sensitive to ϕ than the other modes (1169, 1440, 2878 cm^{-1}). Thus, the phase (η_{max}) of the sensitive Raman modes can be used to determine ϕ. Figure 6g,i shows the plots of ϕ vs ($\eta_{max} - \psi$) for the 1169 and 2878 cm^{-1} peaks, respectively, without consideration of any orientational broadening. The wrapped ($\eta_{max} - \psi$) value can vary between 45° and 135° when ϕ changes from 0° to 180°. The actual value of each tensor element can be different between the interrogated HDPE film and the reported orthorhombic *n*-alkane. However, the overall relation between ($\eta_{max} - \psi$) and ϕ can be used to estimate the range of ϕ from the observed values of ($\eta_{max} - \psi$). Figure 6h shows the histograms of experimentally observed ($\eta_{max} - \psi$) values at 1169 cm^{-1} from all pixels on line ***N*** and line ***B***. Similarly, the histograms of the experimentally observed ($\eta_{max} - \psi$) values at 2878 cm^{-1} are presented in Figure 6j. Interestingly, the histograms of the two frequencies exhibit a narrow distribution of ($\eta_{max} - \psi$) near 90°. The universal narrow distributions of ($\eta_{max} - \psi$) near 90° are represented as the red vertical lines in Figure 6g,j. The crossing points of the vertical lines and the curves of ϕ vs ($\eta_{max} - \psi$) indicate that the ϕ values of the unit cells in the HDPE film are either 0° (= 180°) or 90°, depending on how ϕ is defined.

Determination of $\langle P_2 \rangle$ and $|\theta|$.

From eqs 12–14, three variables (*m*, *n*, *l*) are observable, while four variables (*k*, θ, $\langle P_2 \rangle$, $\langle P_4 \rangle$) are to be determined. Solving this underdetermined problem requires an additional constraint. Thus, we assume an analytical relation between $\langle P_2 \rangle$ and $\langle P_4 \rangle$. Figure 7 shows a few representative models for the relation of $\langle P_2 \rangle$ and $\langle P_4 \rangle$.[54] The von Mises–Fisher model is used to describe the orientation distribution function of electric dipoles in a parallel electric field. $\langle P_2 \rangle$ and $\langle P_4 \rangle$ are calculated by varying κ in $\rho(\beta) \propto e^{\kappa \cos\beta}$, but the relation between $\langle P_2 \rangle$ and $\langle P_4 \rangle$ cannot be expressed in a simple analytical form. The maximum entropy model provides the most probable $\langle P_4 \rangle$ for each $\langle P_2 \rangle$, but is only presentable in complex parametric relations. The Faber model uses an empirical relation of $\log\langle P_4 \rangle = \frac{10}{3}\langle P_2 \rangle$ to describe the fluctuation of the nematic director field. However, the log term makes it challenging to find an analytical solution with eqs 12–14. Interestingly, the three models (von Mises-Fisher, maximum entropy, and Faber) in Figure 7 are relatively close to each other. We find that a single cubic term, $\langle P_4 \rangle = \langle P_2 \rangle^3$, can represent the three popular models for the relation between $\langle P_2 \rangle$ and $\langle P_4 \rangle$. Replacing $\langle P_4 \rangle$ with $\langle P_2 \rangle^3$ in eq 16 yields

$$(36\Omega + 9)\langle P_4\rangle^4 + (12\Omega + 5)\langle P_2\rangle^2 - 15\langle P_2\rangle + \Omega = 0 \quad (17)$$

where $\Omega = (15nl/7m^2)$. eq 17 is a quartic equation for $\langle P_2\rangle$ and analytically solvable. Having $\langle P_2\rangle$ solved, $\langle P_4\rangle$ and $\sin^2\theta$ can also be easily determined from eq 15.

At each image pixel, the coefficients (m, n, l) are determined by fitting the polarization profile of Im{$\chi^{(3)}$} at 1294 cm^{-1} with eq 11. First, $\langle P_2\rangle$ was calculated with eq 17, and then, $\langle P_4\rangle$ and $\sin^2\theta$ were calculated with the cubic relation and eq 15, respectively. Unfortunately, the calculated $\sin^2\theta$ yields only the absolute value of θ with the sign undeterminable. This degeneracy in θ is an inherent limitation of 2D projected optical measurements without tilting the sample.

Figure 7c shows the plot of $|\theta|$ of line ***N***. Interestingly, $|\theta|$ oscillates between 56° and 80° synchronously with ring banding. Similarly, $|\theta|$ along line ***B*** in Figure 7g shows a restricted oscillation between 58° and 80°. The similar $|\theta|$ values of line ***N*** and line ***B*** indicate that the out-of-plane orientation angles are maintained from the nucleation center to the boundary of a PE spherulite. Figure 7d,e show the plots of $\langle P_2\rangle$ and $\langle P_4\rangle$ of line ***N***. Similar to the $|\theta|$ plots, the $\langle P_2\rangle$ and $\langle P_4\rangle$ plots show undulation between 0.7 and 0.9, but their phases are not coherent with that of $|\theta|$. The $\langle P_2\rangle$ and $\langle P_4\rangle$ values of line ***B*** in Figure 7d,e, respectively, exhibit undulation similar to those of line ***N***. The average $\langle P_2\rangle$ value of 0.80 from line ***B*** is slightly lower than that of 0.84 from line ***N***, indicating increased orientational broadening due to the narrower ring banding gaps farther from the nucleation center. It is noted that $|\theta|$ and $\langle P_2\rangle$ remain relatively steady near the nucleation center in line ***N,*** while $|\theta|$ and $\langle P_2\rangle$ are undeterminable at the boundary position in line ***B***.

We evaluate the effect of the analytical model used for $\langle P_2\rangle$ and $\langle P_4\rangle$ by calculating $|\theta|$ and $\langle P_2\rangle$ with a different analytical model. Figure S5 shows the results calculated by the cubic model and a quadratic model. As shown in Figure S5a, the quadratic model, $\langle P_4\rangle = \langle P_2\rangle^2$, is distant from the other representative models compared to the cubic model. Still, the calculated $|\theta|$ and $\langle P_2\rangle$ plots in Figure S5b–e are not significantly different between the cubic and quadratic models, suggesting that accurate selection of an analytical model for $\langle P_2\rangle$ and $\langle P_4\rangle$ is not critical for the output $|\theta|$ and $\langle P_2\rangle$ values. For example, on average, the quadratic model yields lower $|\theta|$ values than the cubic model by 2° and 5° for line ***N*** and line ***B***, respectively.

The ν_{as}(C–C) mode at 1060 cm^{-1} also has the same (B_{1g} + B_{2g}) symmetry as the $\tau(CH_2)$ mode at 1294 cm^{-1}, as shown in Table 1. The polarization profiles of the 1060 cm^{-1} peak are analyzed by the identical method used to analyze the 1294 cm^{-1} peak. In Figure S6, the polarization profiles observed at several locations on line ***N*** show very similar behaviors between the two peaks, and the calculated $|\theta|$ values also show consistent results. The $|\theta|$ plot from the 1060 cm^{-1} peak is slightly lower than that from the 1294 cm^{-1} peak, which may be due to the difference in signal intensity and proximity to neighboring peaks. As shown in Figure 1e,f, the 1060 cm^{-1} peak is weak compared to the neighboring 1126 cm^{-1} peak, while the 1294 cm^{-1} peak is strong and isolated from neighboring peaks. Therefore, the

1294 cm^{-1} peak between the two (B_{1g} + B_{2g}) peaks was used for the 3D orientation angle measurement of PE.

Polarization mixing by tight focusing by a high NA lens can cause a polarization profile to deviate from the analytical model based on all linearly polarized lights. It is extremely challenging to consider the tight focusing effect in the analytical derivation of polarization Raman profiles to express 3D orientation angles and orientational broadening. Instead, we examine focus-induced electric fields associated with a nonlinear susceptibility. As we discussed earlier, nonlinear susceptibility is a fourth-rank tensor for four electric fields (pump, Stokes, probe, and anti-Stokes). Thus, the polarization mixing on an effective nonlinear susceptibility can be estimated by the volume integral of $E_y^2E_x^2$ (and $E_z^2E_x^2$) compared with that of E_x^4 over the focal volume (see the details in the caption of Figure S7). Using the analytical expressions of a focused beam,[58] we calculated the three electric fields near a focus. Figure S7 shows that the ratios of the volume integrals of $E_y^2E_x^2$ and $E_z^2E_x^2$ are 0.00034 and 0.043 to that of E_x^4 when an *x*-polarized beam is focused by a lens with NA = 0.95. We deem the tight focusing effect relatively small compared to the uncertainties from other sources, such as spectral noise and the oversimplification of the $\langle P_2\rangle$–$\langle P_4\rangle$ model. However, the tight focusing effect must be considered for more accurate measurements, particularly when a higher NA objective lens is used.

3D orientation of PE chains on line *N* and line *B*.

Figure 8 illustrates the 3D orientation direction of PE chains on a section of line ***N*** by combining the ψ values (Figure 5d) and the θ values (Figure 7c). The illustrated section covers two banded rings. Because we cannot determine the θ sign, we arbitrarily choose only positive θ for the illustrations. The 3D illustration reconfirms that the out-of-plane angle of chain directions oscillates smoothly up and down within a narrow range across ring bandings. This smooth oscillation with the unchanged sign of θ can be interpreted as a *restricted oscillating lamellar model*, as opposed to the prevailing scheme of a *full twisting lamellar model*, where lamellae twist fully and flip 360° per ring banding. This full twisting lamellar model was supported by SEM images of isolated single lamellar ribbons,[4,5] but full twisting has never been observed directly from lamellar stacks or polymer chains embedded in an intact spherulite.

It needs to be reiterated that, due to the degeneracy in the sign of θ, we cannot directly prove which mechanism of lamellar twisting is correct simply based on the experimental results of polarization-controlled CARS microscopy. However, we can test the full twisting lamellar model by simulating the observed $|\theta|$ near flipping locations. The full twisting lamellar model is supposed to accompany θ sign alternation as ring banding repeats. Figure S8 compares the chain orientations illustrated by the restricted oscillating lamellar model and the full twisting lamellar model. In the full twisting lamellar model (Figure S8c,f), the θ sign of chain directions can be supposed to flip between positive and negative when $|\theta|$ hits the maximum angle (the nearest to the XY plane) per ring banding period. Based on the full twisting lamellar model, the change in θ at the supposed flipping locations is found to be as large as 30° from Figure S8c,f. One can argue that the observed limited $|\theta|$ range might be due to insufficient spatial resolution for fast-flipping chain orientations across the XY plane.

We tested the hypothesis using simulation data with various spatial resolutions. Figure S9 shows synthesized $|\theta|$ from the out-of-plane angle ranging from –50° to 50° as a function of distance over two full twists. The slope of $|\theta|$ vs distance was assumed to be 5 deg/μm from the observed value in Figure 5c for line ***N***. Then, a simple Savitsky–Golay filter was used to smooth the synthesized $|\theta|$ with a window corresponding to the system spatial resolution of 0.5 μm. Figure S9c shows that the smoothed or deconvoluted $|\theta|$ at the supposed flipping location is 89.4°, only 0.6° smaller than the undeconvoluted value. To meet the observed maximum $|\theta|$ of 75° to 80°, we have to increase the smoothing window to 12 or 8 μm, respectively, which is 20 times larger than the spatial resolution. Also, the observed range of $|\theta|$ is similar between line ***N*** and line ***B***, although their ring-to-ring distances (15–20 μm in line ***N***; and 5–10 μm in line ***B***) are different. Thus, the full twisting lamellar model cannot explain the observed smooth oscillations of $|\theta|$ undulations with a large gap from the film plane ($|\theta| = 90°$).

We emphasize that the observed 3D orientation of polymer chains may not be applicable to differently prepared PE spherulites. The film examined in this study was prepared under pressure between glass coverslips during the annealing and cooling processes. In contrast, most polymer samples studied by AFM, SEM, X-ray, and electron diffraction have at least one side of the sample exposed to air. The pressure may have caused a strong perturbation during crystal growth. Also, the thickness of the film (2.1 μm) compared to the spherulite domain size (≈100 μm) and the ring banding periods (5–20 μm) may have affected the resulting chain orientations. Further studies of chain orientations in differently prepared polymer samples will be needed for a better understanding of these complex polymer crystallization phenomena, including lamellar formation, growth, branching, twisting, etc.

CONCLUSION

We have presented the first experimental demonstration of imaging the 3D angles of polymer chain orientation with submicrometer spatial resolution using polarization-controlled BCARS microscopy. We found that a single Raman peak with the ($B_{1g} + B_{2g}$) symmetry could be used to determine the axial angle, $|\theta|$, and the order parameter, $\langle P_2 \rangle$. The 3D orientation results from two line scans crossing a nucleation center and a boundary of PE spherulites strongly suggest that the observed ring banding is more consistent with the restricted oscillating lamellar model than the prevailing model of fully twisting lamellae. In addition to newly available orientation images, BCARS-based imaging provides concentration distribution images maintaining the advantages of BCARS microscopy, such as rapid imaging speed, label-free, fluorescence background-free, versatile polarization control, 3D sectioning, etc. We also emphasize that, in principle, the identical analysis method can be used for spontaneous Raman or stimulated Raman scattering data.

Supplementary Material

Refer to Web version on PubMed Central for supplementary material.

Acknowledgments

The authors thank Anthony Kotula for helping with the HDPE film preparation. They also thank Joy Dunkers for acquiring confocal images and Charlie Camp for discussing on KK phase retrieval.

Data availability

All data used in this article and its supporting information are available from the corresponding author upon reasonable request.

References

(1). Keith HD; Padden FJ Banding in Polyethylene and Other Spherulites. Macromolecules 1996, 29, 7776–7786. DOI: 10.1021/ma960634j.

(2). Lotz B; Miyoshi T; Cheng SZD 50th Anniversary Perspective : Polymer Crystals and Crystallization: Personal Journeys in a Challenging Research Field. Macromolecules 2017, 50, 5995–6025. DOI: 10.1021/acs.macromol.7b00907.

(3). Lovinger AJ Twisted Crystals and the Origin of Banding in Spherulites of Semicrystalline Polymers. Macromolecules 2020, 53 (3), 741–745. DOI: 10.1021/acs.macromol.9b01567.

(4). Kunz M; Dreschsler M; Möller M On the structure of ultra-high molecular weight polyethylene gels. Polymer 1995, 36 (7), 1331–1339. DOI: 10.1016/0032-3861(95)95909-K.

(5). Olley RH; Hodge AM; Bassett DC A permanganic etchant for polyolefines. J. Polym. Sci.: Polym. Phys. Ed. 1979, 17 (4), 627–643. DOI: 10.1002/pol.1979.180170406.

(6). King A; Johnson G; Engelberg D; Ludwig W; Marrow J Observations of Intergranular Stress Corrosion Cracking in a Grain-Mapped Polycrystal. Science 2008, 321 (5887), 382–385. DOI: 10.1126/science.1156211. [PubMed: 18635797]

(7). Viganò N; Ludwig W X-ray orientation microscopy using topo-tomography and multi-mode diffraction contrast tomography. Curr. Opin. Solid State Mater. Sci. 2020, 24 (4), 100832–100832. DOI: 10.1016/j.cossms.2020.100832.

(8). Liu HH; Schmidt S; Poulsen HF; Godfrey A; Liu ZQ; Sharon JA; Huang X Three-Dimensional Orientation Mapping in the Transmission Electron Microscope. Science 2011, 332 (6031), 833–834. DOI: 10.1126/science.1202202. [PubMed: 21566190]

(9). Eggeman AS; Krakow R; Midgley PA Scanning precession electron tomography for three-dimensional nanoscale orientation imaging and crystallographic analysis. Nat. Commun. 2015, 6 (1), 7267–7267. DOI: 10.1038/ncomms8267. [PubMed: 26028514]

(10). Richard-lacroix M; Pellerin C Accurate New Method for Molecular Orientation Quantification Using Polarized Raman Spectroscopy. Macromolecules 2013, 46, 5561–5569. DOI: 10.1021/ma400955u.

(11). Chang W-S; Ha JW; Slaughter LS; Link S Plasmonic nanorod absorbers as orientation sensors. Proc. Natl. Acad. Sci. U.S.A. 2010, 107, 2781–2786. DOI: 10.1073/pnas.0910127107. [PubMed: 20133646]

(12). Prokhorov VV; Pozin SI; Perelygina OM; Mal'Tsev EI Crystallography and Molecular Arrangement of Polymorphic Monolayer J-Aggregates of a Cyanine Dye: Multiangle Polarized Light Fluorescence Optical Microscopy Study. Langmuir 2018, 34, 4803–4810. DOI: 10.1021/acs.langmuir.8b01008. [PubMed: 29601203]

(13). Mazumder N; Balla NK; Zhuo GY; Kistenev YV; Kumar R; Kao FJ; Brasselet S; Nikolaev VV; Krivova NA Label-Free Nonlinear Multimodal Optical Microscopy—Basics, Development, and Applications. Front. Phys 2019, 7, 1–26. DOI: 10.3389/fphy.2019.00170.

(14). Koziol P; Liberda D; Kwiatek WM; Wrobel TP Macromolecular Orientation in Biological Tissues Using a Four-Polarization Method in FT-IR Imaging. Anal. Chem. 2020, 92, 13313–13318. DOI: 10.1021/acs.analchem.0c02591. [PubMed: 32854498]

(15). Kossack W; Kremer F Banded spherulites and twisting lamellae in poly-ε-caprolactone. Colloid. Polym. Sci. 2019, 297, 771–779. DOI: 10.1007/s00396-019-04503-8.

(16). Mukherjee P; Ghosh A; Spegazzini N; Lamborn MJ; Monwar MM; Deslauriers PJ; Bhargava R Relating Post-yield Mechanical Behavior in Polyethylenes to Spatially Varying Molecular Deformation Using Infrared Spectroscopic Imaging: Homopolymers. Macromolecules 2018, 51, 3836–3844. DOI: 10.1021/acs.macromol.8b00363.

(17). Cleff C; Gasecka A; Ferrand P; Rigneault H; Brasselet S; Duboisset J Direct imaging of molecular symmetry by coherent anti-stokes Raman scattering. Nat. Commun. 2016, 7, 1–7. DOI: 10.1038/ncomms11562.

(18). Kennedy AP; Sutcliffe J; Cheng JX Molecular composition and orientation in myelin figures characterized by coherent anti-stokes Raman scattering microscopy. Langmuir 2005, 21 (14), 6478–6486. [PubMed: 15982056]

(19). Lee YJ; Snyder CR; Forster AM; Cicerone MT; Wu W.-l. Imaging the Molecular Structure of Polyethylene Blends with Broadband Coherent Raman Microscopy. ACS Macro Lett. 2012, 1, 1347–1351. DOI: 10.1021/mz300546e. [PubMed: 35607170]

(20). Wu JX; Mao NN; Xie LM; Xu H; Zhang J Identifying the Crystalline Orientation of Black Phosphorus Using Angle-Resolved Polarized Raman Spectroscopy. Angewandte Chemie-International Edition 2015, 54 (8), 2366–2369. DOI: 10.1002/anie.201410108. [PubMed: 25611334]

(21). Presser V; Schuster BE; Casu MB; Heinemeyer U; Schreiber F; Nickel KG; Chassé T Raman polarization studies of highly oriented organic thin films. Journal of Raman Spectroscopy 2009, 40 (12), 2015–2022. DOI: 10.1002/jrs.2361.

(22). Citra MJ; Chase DB; Ikeda RM; Gardner KH Molecular-Orientation of High-Density Polyethylene Fibers Characterized By Polarized Raman-Spectroscopy. Macromolecules 1995, 28, 4007–4012. DOI: 10.1021/ma00115a037.

(23). Hikima Y; Morikawa J; Hashimoto T FT-IR image processing algorithms for in-plane orientation function and azimuth angle of uniaxially drawn polyethylene composite film. Macromolecules 2011, 44, 3950–3957. DOI: 10.1021/ma2003129.

(24). Lu F; Zheng W; Huang Z Coherent anti-Stokes Raman scattering microscopy using tightly focused radially polarized light. Opt. Lett. 2009, 34 (12), 1870–1872. DOI: 10.1364/ol.34.001870. [PubMed: 19529731]

(25). Saito Y; Kobayashi M; Hiraga D; Fujita K; Kawano S; Smith NI; Inouye Y; Kawata S z-Polarization sensitive detection in micro-Raman spectroscopy by radially polarized incident light. Journal of Raman Spectroscopy 2008, 39 (11), 1643–1648. DOI: 10.1002/jrs.1953.

(26). Mino T; Saito Y; Yoshida H; Kawata S; Verma P Molecular orientation analysis of organic thin films by z-polarization Raman microscope. Journal of Raman Spectroscopy 2012, 43 (12), 2029–2034. DOI: 10.1002/jrs.4118.

(27). Toprak E; Enderlein J; Syed S; McKinney SA; Petschek RG; Ha T; Goldman YE; Selvin PR Defocused orientation and position imaging (DOPI) of myosin V. Proc. Natl. Acad. Sci. U.S.A. 2006, 103, 6495–6499. DOI: 10.1073/pnas.0507134103. [PubMed: 16614073]

(28). Wang M; Marr JM; Davanco M; Gilman JW; Liddle JA Nanoscale deformation in polymers revealed by single-molecule super-resolution localization-orientation microscopy. Mater. Horiz. 2019, 6, 817–825. DOI: 10.1039/c8mh01187g.

(29). Empedocles SA; Neuhauser R; Bawendi MG Three-dimensional orientation measurements of symmetric single chromophores using polarization microscopy. Nature 1999, 399, 126–130. DOI: 10.1038/20138.

(30). Lee YJ Concurrent polarization IR analysis to determine the 3D angles and the order parameter for molecular orientation imaging. Opt. Express 2018, 26, 24577–24590. DOI: 10.1364/OE.26.024577. [PubMed: 30469571]

(31). Xu S; Rowlette J; Lee YJ Imaging 3D molecular orientation by orthogonal-pair polarization IR microscopy. Opt. Express 2022, 30 (6), 8436–8447. DOI: 10.1364/OE.449667. [PubMed: 35299296]

(32). Xu S; Snyder CR; Rowlette J; Lee YJ Three-Dimensional Molecular Orientation Imaging of a Semicrystalline Polymer Film under Shear Deformation. Macromolecules 2022, 55 (7), 2627–2635. DOI: 10.1021/acs.macromol.1c02036.

(33). Hopkins JB; Farrow LA Raman microprobe determination of local crystal orientation. J. Appl. Phys. 1986, 59 (4), 1103–1110. DOI: 10.1063/1.336547.

(34). Wu J; Zhang D; Lu Q; Gutierrez HR; Eklund PC Polarized Raman scattering from single GaP nanowires. Phys. Rev. B 2010, 81 (16), 165415. DOI: 10.1103/PhysRevB.81.165415.

(35). Ilchenko O; Pilgun Y; Kutsyk A; Bachmann F; Slipets R; Todeschini M; Okeyo PO; Poulsen HF; Boisen A Fast and quantitative 2D and 3D orientation mapping using Raman microscopy. Nat. Commun. 2019, 10, 5555. DOI: 10.1038/s41467-019-13504-8. [PubMed: 31804493]

(36). Galvis L; Dunlop JWC; Duda G; Fratzl P; Masic A Polarized Raman Anisotropic Response of Collagen in Tendon: Towards 3D Orientation Mapping of Collagen in Tissues. PLoS One 2013, 8 (5), e63518. DOI: 10.1371/journal.pone.0063518. [PubMed: 23691057]

(37). Schrof S; Varga P; Galvis L; Raum K; Masic A 3D Raman mapping of the collagen fibril orientation in human osteonal lamellae. J. Struct. Biol. 2014, 187 (3), 266–275. DOI: 10.1016/j.jsb.2014.07.001. [PubMed: 25025981]

(38). Lee YJ Determination of 3D molecular orientation by concurrent polarization analysis of multiple Raman modes in broadband CARS spectroscopy. Opt. Express 2015, 23, 29279–29295. DOI: 10.1364/OE.23.029279. [PubMed: 26561197]

(39). Kobayashi M; Tadokoro H; Porter RS Polarized Raman spectra of n-alkane single crystals with orthorhombic polyethylene-type sublattice. J. Chem. Phys. 1980, 73, 3635–3642. DOI: 10.1063/1.440590.

(40). Pigeon M; Prud'homme RE; Pezolet M Characterization of molecular orientation in polyethylene by Raman spectroscopy. Macromolecules 1991, 24, 5687–5694.

(41). Takahashi Y; Puppulin L; Zhu W; Pezzotti G Raman tensor analysis of ultra-high molecular weight polyethylene and its application to study retrieved hip joint components. Acta Biomater. 2010, 6 (9), 3583–3594. DOI: 10.1016/j.actbio.2010.02.051. [PubMed: 20215056]

(42). Bower DI Orientation distribution functions for uniaxially oriented polymers. J. Polym. Sci.: Polym. Phys. Ed. 1981, 19, 93–107. DOI: 10.1002/pol.1981.180190108.

(43). Abbate S; Zerbi G; Wunder SL Fermi resonances and vibrational spectra of crystalline and amorphous polyethylene chains. J. Phys. Chem. 1982, 86, 3140–3149.

(44). Kotula AP; Meyer MW; De Vito F; Plog J; Hight Walker AR; Migler KB The rheo-Raman microscope: Simultaneous chemical, conformational, mechanical, and microstructural measures of soft materials. Rev. Sci. Instrum. 2016, 87, 105105. DOI: 10.1063/1.4963746. [PubMed: 27802720]

(45). Chon B; Truong J; Hansen M; Hahm J.-i.; Lee YJ Position- and Polarization-Specific Waveguiding of Multi-Emissions in Single ZnO Nanorods. ACS Photon. 2019, 6, 1416–1424. DOI: 10.1021/acsphotonics.8b01763.

(46). Ryu IS; Camp CH; Jin Y; Cicerone MT; Lee YJ; Camp CH Jr; Jin Y; Cicerone MT; Lee YJ Beam scanning for rapid coherent Raman hyperspectral imaging. Opt. Lett. 2015, 40 (24), 5826–5829. DOI: 10.1364/ol.40.005826. [PubMed: 26670522]

(47). Liu Y; Lee YJ; Cicerone MT Broadband CARS spectral phase retrieval using a time-domain Kramers-Kronig transform. Opt. Lett. 2009, 34, 1363–1365. DOI: 10.1364/OL.34.001363. [PubMed: 19412273]

(48). Camp CH Jr; Bender JS; Lee YJ Real-time and high-throughput Raman signal extraction and processing in CARS hyperspectral imaging. Opt. Express 2020, 28 (14), 20422–20422. DOI: 10.1364/OE.397606. [PubMed: 32680102]

(49). Eesley GL Coherent Raman Spectroscopy; Pergamon Press, 1981.

(50). Masetti G; Abbate S; Gussoni M; Zerbi G Raman intensities of stretch oriented polyethylene and perdeuteropolyethylene. I. Experiments. J. Chem. Phys. 1980, 73, 4671–4679. DOI: doi:10.1063/1.440660.

(51). Avitabile G; Napolitano R; Pirozzi B; Rouse KD; Thomas MW; Willis BTM Low temperature crystal structure of polyethylene: Results from a neutron diffraction study and from potential energy calculations. J. Polym. Sci.: Polym. Lett. Ed. 1975, 13 (6), 351–355. DOI: 10.1002/pol.1975.130130607.

(52). Lorenzen M; Hanfland M High-Resolution X-ray Powder Diffraction Studies of Polyethylene and Ethylene–Octene Copolymers: The Setting Angle. Macromolecules 2003, 36 (16), 6095–6099. DOI: 10.1021/ma0214411.

(53). Strobl GR; Hagedorn W Raman spectroscopic method for determining the crystallinity of polyethylene. J. Polym. Sci.: Polym. Phys. Ed. 1978, 16, 1181–1193. DOI: 10.1002/pol.1978.180160704.

(54). Würflinger A; Urban S Relations between Nematic Potential and Order Parameters <P2> and <P4>. Z. Naturforsch. A 1998, 53, 883–886. DOI: 10.1515/zna-1998-10-1112.

(55). Khatri C; Mardia K The von Mises-Fisher matrix distribution in orientation statistics. J. Roy. Stat. Soc. Ser. B 1977, 39, 95–106. DOI: 10.2307/2984884.

(56). Lagugné Labarthet F; Buffeteau T; Sourisseau C Orientation distribution functions in uniaxial systems centered perpendicularly to a constraint direction. Appl. Spectrosc. 2000, 54 (5), 699–705. DOI: 10.1366/0003702001949951.

(57). Faber TE A continuum theory of disorder in nematic liquid crystals. I. Proc. R. Soc. Lond. A. Math. Phys. Sci. 1977, 353 (1673), 247–259. DOI: 10.1098/rspa.1977.0032.

(58). Boivin A; Wolf E Electromagnetic Field in the Neighborhood of the Focus of a Coherent Beam. Phys. Rev. 1965, 138 (6B), B1561–B1565. DOI: 10.1103/PhysRev.138.B1561.

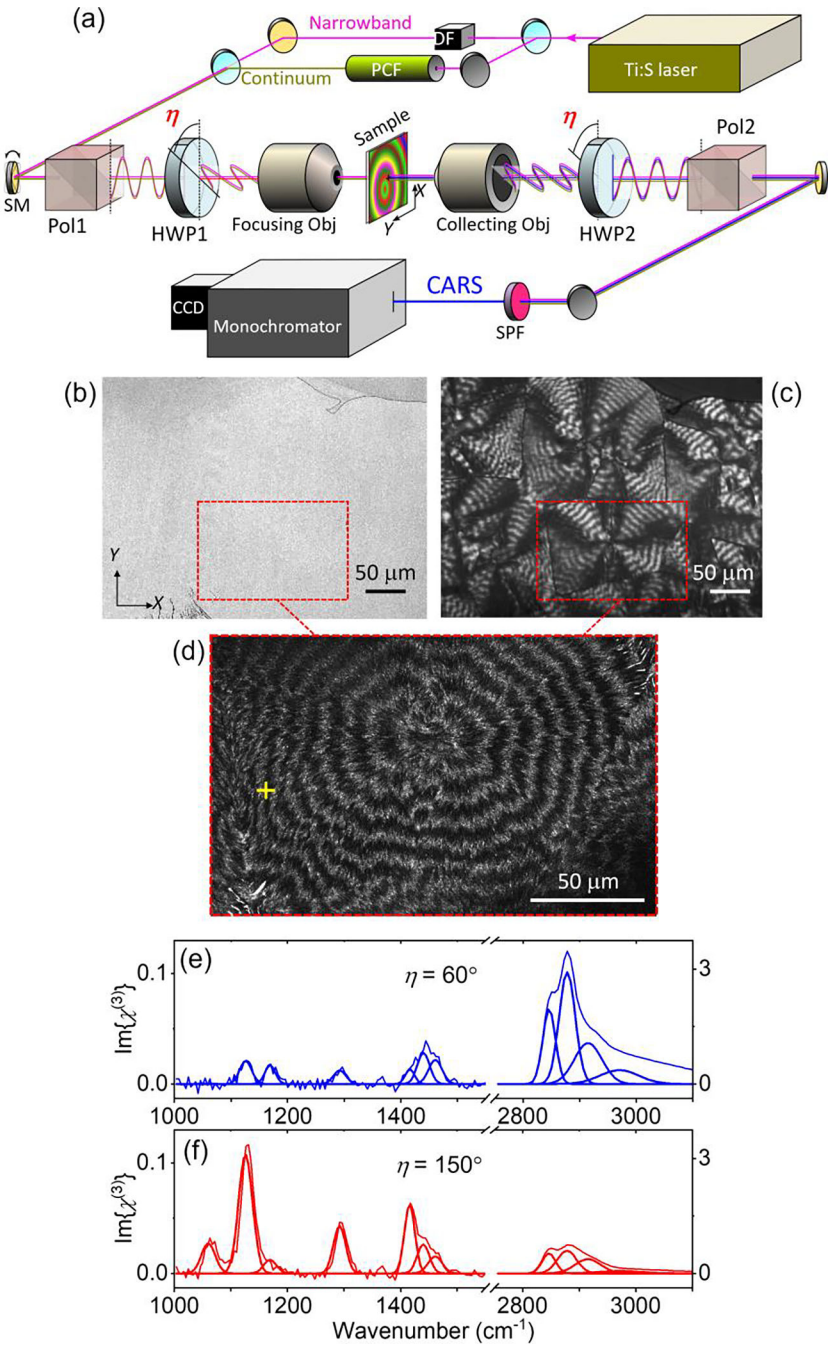

Figure 1.

Polarization-controlled broadband coherent anti-Stokes Raman scattering (BCARS) imaging of an HDPE film. (a) Schematic illustration of the polarization-controlled BCARS system. See the text for details. (b) Bright-field image and (c) polarization optical microscopy (POM) image of the identical region of an HDPE film. (d) Enlarged confocal scattering image of the rectangular area in panels (b,c). (e,f) Im{$\chi^{(3)}$} spectra retrieved by the Kramers–Kronig method from raw BCARS spectra acquired by two polarization excitation angles at the (+) marked location in panel (d).

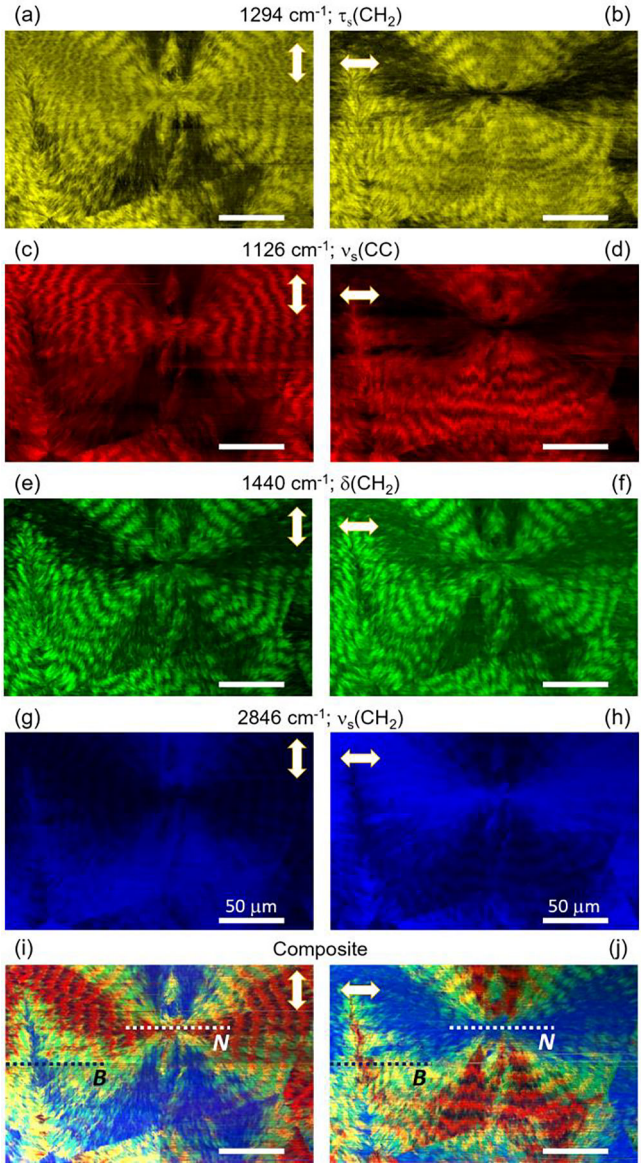

Figure 2.

Im{$\chi^{(3)}$} images of the HDPE film constructed by different Raman modes and their composite images. Left column: *Y*-polarized excitation ($\eta = 90°$). Right column: *X*-polarized excitation ($\eta = 0°$). Line ***N*** and line ***B*** cross a nucleation center and a spherulite boundary, respectively. The two lines were analyzed further by polarization profile measurements followed by a detailed 3D orientational angle analysis.

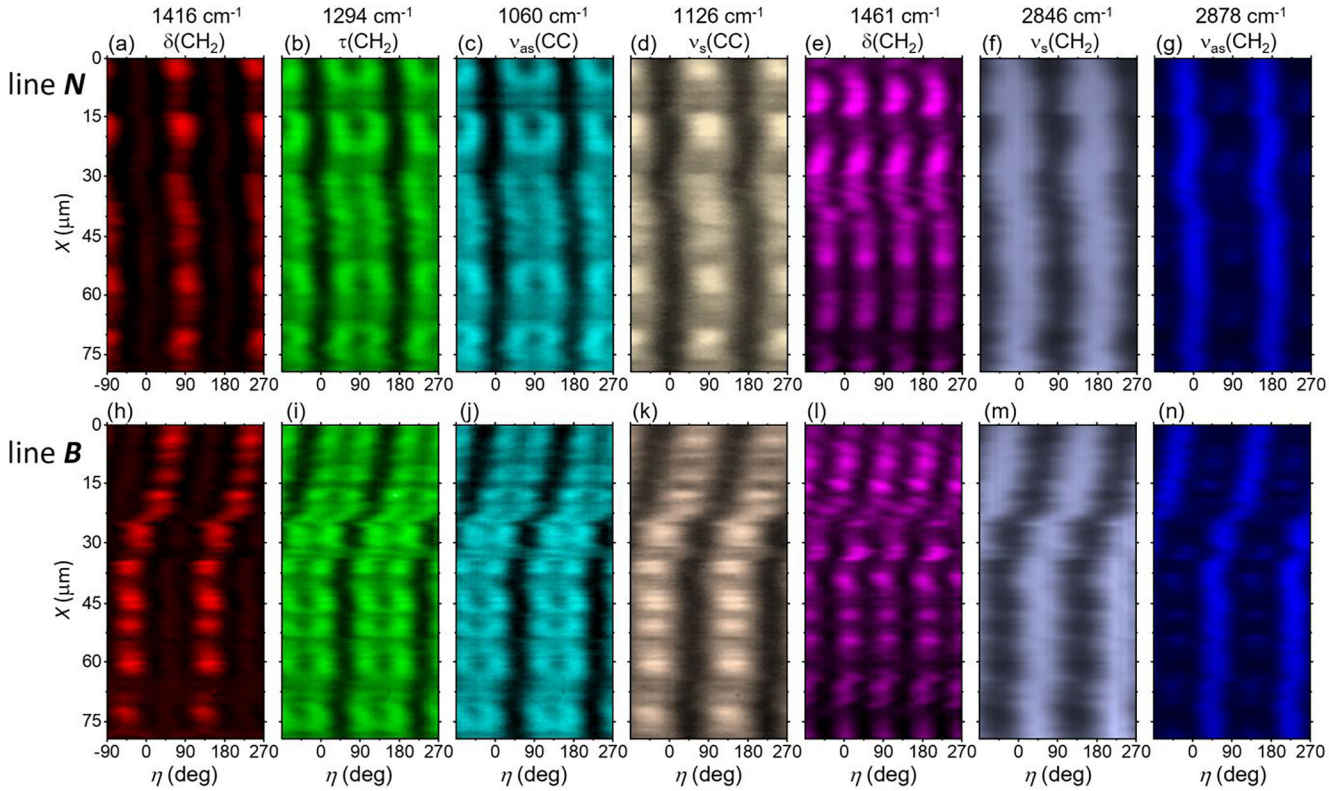

Figure 3.

Contour map of Im{$\chi^{(3)}$} for various Raman modes as a function of polarization angle and distance on line ***N*** and line ***B***. The intensity of each contour plot was scaled from zero to its maximum.

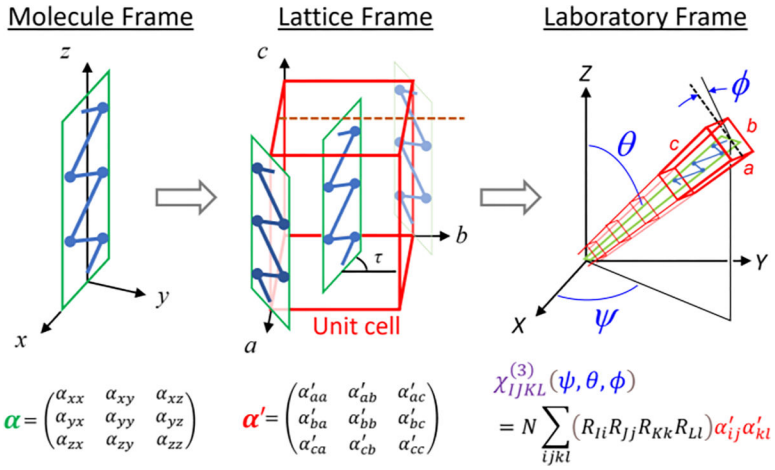

Figure 4.

Schematic illustration of Raman polarizabilities at different frames. The molecular Raman polarizability (α) is defined in the molecule frame of (x,y,z). The molecular plane of the C–C chain is in the xz plane. The lattice Raman polarizability (α') is defined in the lattice frame of (a,b,c). The molecular plane is tilted by the setting angle τ from the b axis in the unit cell. The third-order nonlinear susceptibility ($\chi^{(3)}$) is defined in the laboratory frame of (X,Y,Z). The lattice orientation in the laboratory frame can be described by the 3D Euler angles: the azimuthal angle (ψ), the rotational angle (ϕ), and the axial angle (θ).

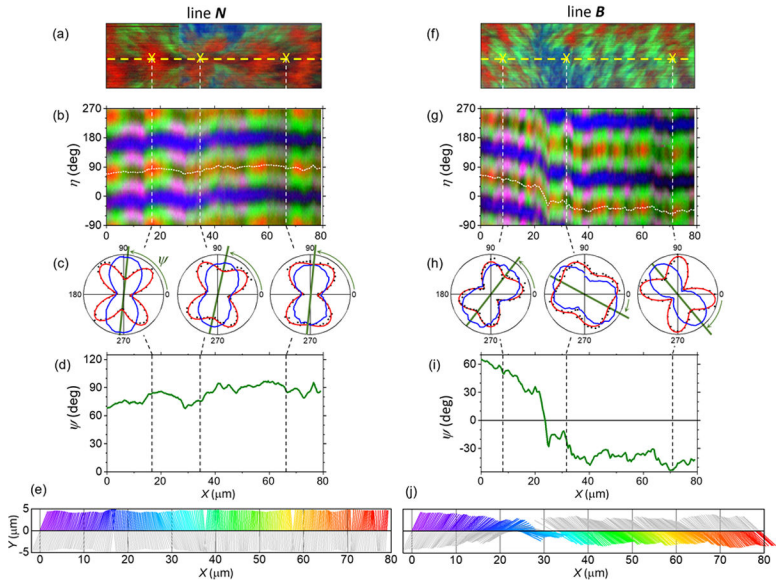

Figure 5.

Determination of ψ. (a) Im$\{\chi^{(3)}\}$ image near line ***N*** from Figure 2i. (b) Polarization dependent Im$\{\chi^{(3)}\}$ of line ***N***, composed of (red) 1416 cm^{-1}, (blue) 2878 cm^{-1}, (green) 1294 cm^{-1}, and (magenta) 1461 cm^{-1}. (c) Polar plots of Im$\{\chi^{(3)}\}$ of the (red) 1294 cm^{-1} and (blue) 1126 cm^{-1} peaks at three marked locations. The ψ angle was denoted by the angle of the common symmetry axis of the polar plots. (d) Plot of ψ for line ***N***. (e) Corresponding chain orientations projected to the XY plane of line ***N***. (f–j) Same analysis of polarization-dependent Im$\{\chi^{(3)}\}$ and ψ determination for line ***B***.

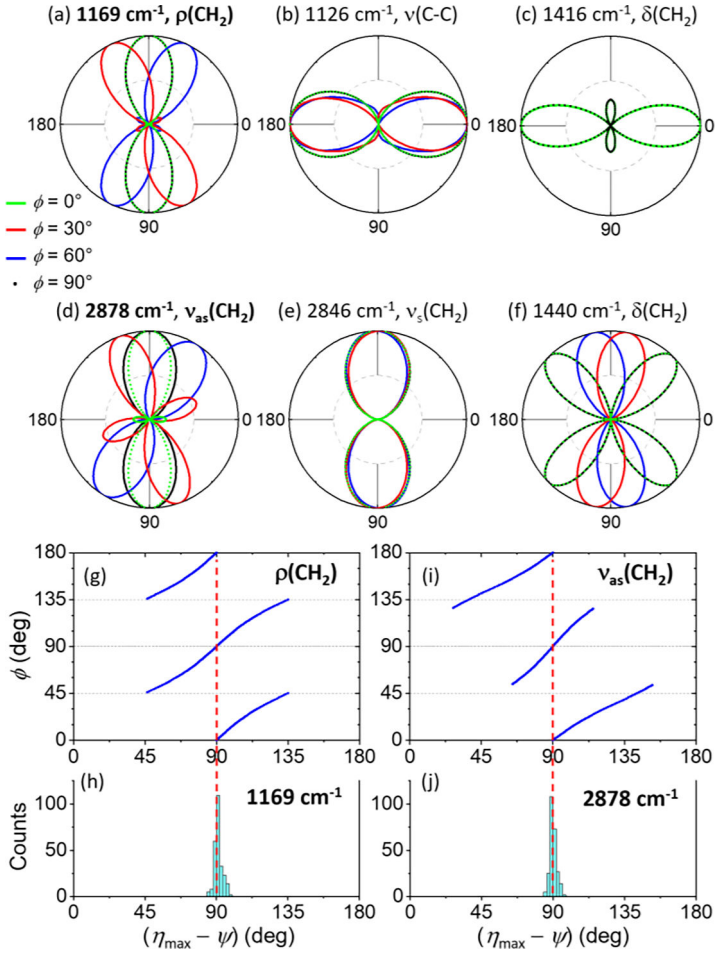

Figure 6.

Determination of ϕ. (a–f) Polarization-dependent $\chi^{(3)}_{\text{eff}}$ simulated for six Raman modes for various ϕ values for $\psi = 0°$ and $\theta = 65°$. The $\chi^{(3)}_{\text{eff}}$ was calculated using the tensor elements in Table S1, and normalized by the maximum value. η_{max} was defined as the η value corresponding to the maximum $\chi^{(3)}_{\text{eff}}$. Thus, η_{max} was calculated for ϕ. (g) Plot of ϕ vs η_{max} from the simulated $\chi^{(3)}_{\text{eff}}$ for the $\rho(CH_2)$ mode. (h) Histogram of $(\eta_{\text{max}} - \psi)$ for the experimental $\text{Im}\{\chi^{(3)}\}$ peak at 1169 cm^{-1} from the image pixels of line ***N*** and line ***B***, where ψ is from Figure 5d,i. (i) Plot of ϕ vs η_{max} from the simulated $\chi^{(3)}_{\text{eff}}$ for the $\nu_{as}(CH_2)$ mode. (j) Histogram of $(\eta_{\text{max}} - \psi)$ for the experimental $\text{Im}\{\chi^{(3)}\}$ peak at 2878 cm^{-1}.

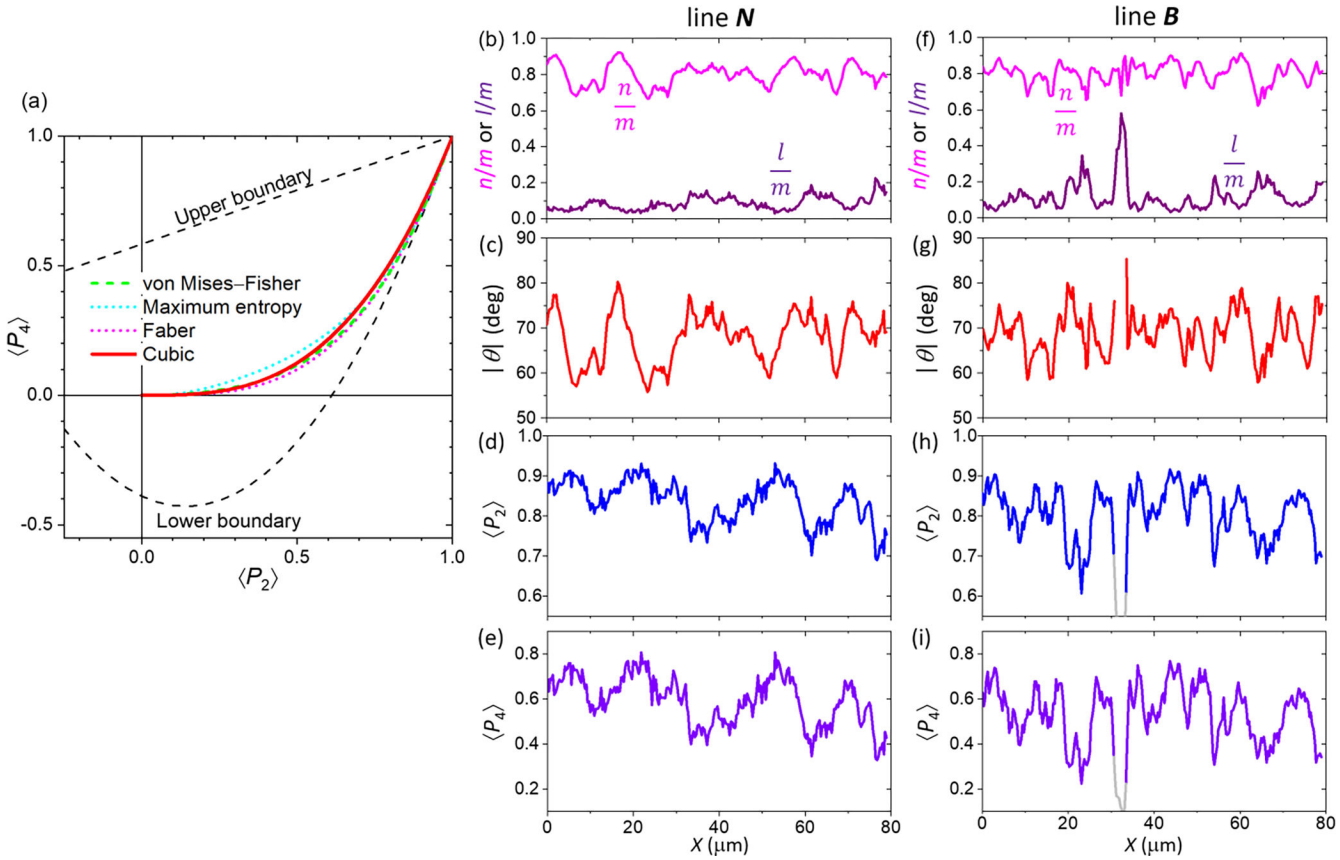

Figure 7.

Determination of $|\theta|$, $\langle P_2\rangle$, and $\langle P_4\rangle$. (a) Relations between $\langle P_2\rangle$ and $\langle P_4\rangle$ from various models. The black dashed lines indicate the upper and the lower boundaries limited by the Schwartz inequality.[42] The von Mises–Fisher model assumes that $\rho(\beta) \propto e^{\kappa\cos\beta}$.[55] The maximum entropy model provides the most probable $\langle P_4\rangle$ for each $\langle P_2\rangle$.[42,56] The Faber model assumes $\log\langle P_4\rangle = \frac{10}{3}\langle P_2\rangle$.[57] The cubic model assumes $\langle P_4\rangle = \langle P_2\rangle^3$. (b) Ratios of the coefficients (m, n, l) determined by fitting the observed polarization-dependent Im$\{\chi^{(3)}\}$ at 1294 cm^{-1} from line ***N*** using eq 11. (c–e) $|\theta|$, $\langle P_2\rangle$, and $\langle P_4\rangle$ calculated using the coefficient ratios in (b) with eqs 15 and 16 assuming the cubic model for the $\langle P_2\rangle$–$\langle P_4\rangle$ relation. (f–i) Determination of $|\theta|$, $\langle P_2\rangle$, and $\langle P_4\rangle$ for line ***B***.

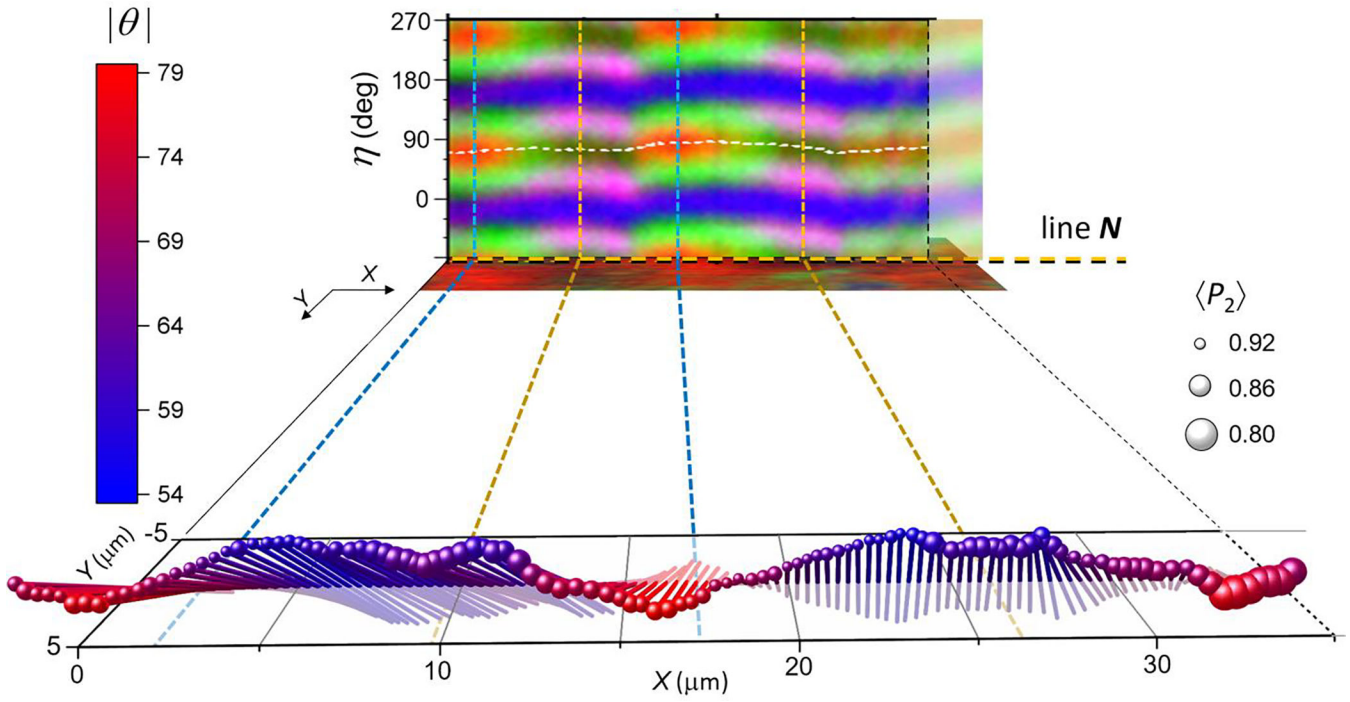

Figure 8.

Illustration of 3D chain orientations. A section corresponding to two banded rings was highlighted from line ***N***. In the back, a part of the polarization-dependent Im{$\chi^{(3)}$} image was extracted from Figure 5b. In the front, 3D directions of PE chains were illustrated using ψ values from Figure 5d and the $|\theta|$ values from Figure 7c. The color of a rod indicates $|\theta|$, and the symbol size represents $\langle P_2 \rangle$, as indicated. For illustration, restricted oscillating for $\theta > 0$ was assumed.

Table 1.

Peak Assignment, the Corresponding Group Symmetry, and the Raman Tensor Elements of Orthorhombic PE.[39–42,50]

Frequency (cm^{-1})	Mode	Symmetry [a]
1060	ν_{as}(C–C)	$B_{1g} + B_{2g}$
1126	ν_{s}(C–C)	$A_g + B_{3g}$
1169	$\rho(CH_2)$	$A_g + B_{3g}$
1294	$\tau(CH_2)$	$B_{1g} + B_{2g}$
1416	$\delta(CH_2)$	A_g
1440	$\delta(CH_2)$	B_{3g} (+ A_g)[b]
1461	$\delta(CH_2)$	B_{3g} (+ A_g)[b]
2846	$\nu_{s}(CH_2)$	$A_g + B_{3g}$
2878	$\nu_{as}(CH_2)$	$A_g + B_{3g}$

[a] ν_{as}, asymmetric stretching; ν_{s}, symmetric stretching; ρ, rocking; δ, scissoring; and τ, twisting.

[b] Possible Fermi resonance.[40]

Table 2.

Raman Tensor Elements Corresponding to the Four Symmetries for the Orthorhombic PE.[39,a]

Symmetry	a'	$\chi^{(3)}_{\mathbf{eff}}$
A_g	$\begin{pmatrix} p & 0 & 0 \\ 0 & q & 0 \\ 0 & 0 & r \end{pmatrix}$	$\{\cos^2\eta\,[\cos^2\theta(p\cos^2\phi + q\sin^2\phi) + r\sin^2\theta] + \sin\eta\cos\eta[(p-q)\cos\theta\sin(2\phi)] + \sin^2\eta\,[p\sin^2\phi + q\cos^2\phi]\}^2$
B_{1g}	$\begin{pmatrix} 0 & 0 & 0 \\ 0 & 0 & e \\ 0 & e & 0 \end{pmatrix}$	$4e^2\cos^2\eta\,\sin^2\theta(\cos\eta\cos\theta\sin\phi - \sin\eta\cos\phi)^2$
B_{2g}	$\begin{pmatrix} 0 & 0 & f \\ 0 & 0 & 0 \\ f & 0 & 0 \end{pmatrix}$	$4f^2\cos^2\eta\,\sin^2\theta(\cos\eta\cos\theta\cos\phi + \sin\eta\sin\phi)^2$
B_{3g}	$\begin{pmatrix} 0 & d & 0 \\ d & 0 & 0 \\ 0 & 0 & 0 \end{pmatrix}$	$4d^2[(\sin^2\eta - \cos^2\eta\cos^2\theta)\sin(2\phi) + \sin(2\eta)\cos\theta\,\cos(2\phi)]^2$

[a]The effective nonlinear susceptibility, $\chi^{(3)}_{\mathbf{eff}}$, is expressed as a function of η, where $(\eta - \psi)$ is replaced with η for simplicity.